Research Article | Vol. 30, No. 26 / 19 Dec 2022 / Optics Express 46040
Optics EXPRESS

Parity-pair-mixing effects in nonlinear spectroscopy of HDO

MEISSA L. DIOUF,[1] ROLAND TÓBIÁS,[2] FRANK M. J. COZIJN,[1] EDCEL J. SALUMBIDES,[1] CSABA FÁBRI,[2] CRISTINA PUZZARINI,[3] ATTILA G. CSÁSZÁR,[2,4] AND WIM UBACHS[1,*]

[1]*Department of Physics and Astronomy, LaserLaB, Vrije Universiteit, De Boelelaan 1081, 1081 HV Amsterdam, The Netherlands*
[2]*Laboratory of Molecular Structure and Dynamics, Institute of Chemistry, ELTE Eötvös Loránd University and MTA-ELTE Complex Chemical Systems Research Group, H-1117 Budapest, Pázmány Péter sétány 1/A, Hungary*
[3]*Dipartimento di Chimica "Giacomo Ciamician", Universitá di Bologna, Via F. Selmi 2, I-40126 Bologna, Italy*
[4]*attila.csaszar@ttk.elte.hu*
[*]*w.m.g.ubachs@vu.nl*

Abstract: A non-linear spectroscopic study of the HDO molecule is performed in the wavelength range of 1.36–1.42 μm using noise-immune cavity-enhanced optical-heterodyne molecular spectroscopy (NICE-OHMS). More than 100 rovibrational Lamb dips are recorded, with an experimental precision of 2–20 kHz, related to the first overtone of the O–H stretch fundamental of $HD^{16}O$ and $HD^{18}O$. Significant perturbations, including distortions, shifts, and splittings, have been observed for a number of Lamb dips. These spectral perturbations are traced back to an AC-Stark effect, arising due to the strong laser field applied in *all* saturation-spectroscopy experiments. The AC-Stark effect mixes parity pairs, that is pairs of rovibrational states whose assignment differs solely in the K_c quantum number, where K_c is part of the standard J_{K_a,K_c} asymmetric-top rotational label. Parity-pair mixing seems to be especially large for parity pairs with $K_a \geq 3$, whereby their energy splittings become as small as a few MHz, resulting in multi-component asymmetric Lamb-dip profiles of gradually increasing complexity. These complex profiles often include crossover resonances. This effect is well known in saturation spectroscopy, but has not been reported in combination with parity-pair mixing. Parity-pair mixing is not seen in $H_2^{16}O$ and $H_2^{18}O$, because their parity pairs correspond to *ortho* and *para* nuclear-spin isomers, whose interaction is prohibited. Despite the frequency shifts observed for $HD^{16}O$ and $HD^{18}O$, the absolute accuracy of the detected transitions still exceeds that achievable by Doppler-limited techniques.

1. Introduction

Most studies dealing with gas-phase rovibrational spectroscopy of small molecules utilize direct linear absorption and Fourier-transform spectroscopy [1]. In these measurements, the spectral resolution is severely limited by Doppler broadening. This situation can be improved significantly by employing saturation techniques of nonlinear spectroscopy [2]. The application of saturation techniques has the advantage that the linewidth, typically several hundred MHz under Doppler-broadened conditions, reduces to the sub-MHz regime. Saturation techniques combined with frequency-comb-based calibration, like noise-immune cavity-enhanced optical-heterodyne molecular spectroscopy (NICE-OHMS, see Refs. 3 and 4), can reach a spectral uncertainty below 10 kHz [5–15]. This accuracy represents an improvement over 2–3 orders of magnitude in the determination of line centers.

#474525 https://doi.org/10.1364/OE.474525
Journal © 2022 Received 30 Aug 2022; revised 27 Oct 2022; accepted 27 Oct 2022; published 5 Dec 2022

Optics EXPRESS

Based on the successful application of our NICE-OHMS apparatus [16,17] to study the rovibrational energy-level structure of two permutationally symmetric water isotopologues, $H_2{}^{16}O$ [9,13] and $H_2{}^{18}O$ [10], the principal objective of the present paper has been to conduct NICE-OHMS measurements on $HD^{16}O$. This investigation was designed to obtain accurate pure rotational energies for this permutationally nonsymmetric water isotopologue. Nevertheless, there is an important, symmetry-related difference between the spectroscopy of H_2O and HDO. Since H_2O isotopologues contain two equivalent H nuclei, these species have two nuclear-spin isomers, called *ortho* and *para*, and the interaction between the *ortho* and *para* states is symmetry forbidden. In contrast, HDO isotopologues have a single nuclear-spin isomer, allowing the interaction of close-lying rovibrational states of opposite parity, which may become mixed under the perturbing influence of external electric fields. The extent of such interactions under conditions of saturation spectroscopy has not been explored so far and thus its magnitude has remained unknown.

Our experimental campaign yielded more than 100 Lamb-dip features, involving states in the first overtone of the O–H stretch fundamental of $HD^{16}O$, with an experimental precision of 2–20 kHz. For transitions whose upper and/or lower states have K_a>3, multi-component Lamb-dip profiles have been identified (K_a is part of the standard J_{K_a,K_c} asymmetric-top rotational label [18]). Even for single Lamb dips, frequency shifts on the order of 100 kHz were detected through a comparison of the experimental (NICE-OHMS-based) energy splittings with their counterparts derived from an effective Hamiltonian (EH) model [19]. The complex Lamb-dip profiles and the frequency shifts are explained with mixing between nearby parity pairs, that is pairs of opposite-parity rovibrational states differing only in their K_c values. To prove this interpretation, benchmark experiments have been performed for $HD^{18}O$, $H_2{}^{16}O$, and $H_2{}^{18}O$, as well, confirming that for transitions with the same lower and upper states (a) no spectral distortions are discernible in the Lamb-dip profiles of $H_2{}^{16}O$ and $H_2{}^{18}O$, and (b) $HD^{18}O$ exhibits similar complex Lamb-dip profiles as $HD^{16}O$.

2. Methodological details

2.1. NICE-OHMS measurements

A NICE-OHMS apparatus, shown schematically in Fig. 1 and described in Refs. 9 and 16, is used to record selected absorption lines of $HD^{16}O$ and other water isotopologues, under saturation conditions. NICE-OHMS is a special form of cavity-enhanced absorption spectroscopy (CEAS, see Ref. 20), endowed with extreme sensitivity [3,4,21,22]. In our setup, a double modulation scheme is included *via* an electro-optic modulator (EOM) for imposing sideband modulations to the central carrier frequency. A low-frequency modulation at 20 MHz is employed for Pound–Drever–Hall (PDH) locking of the laser to the optical cavity with a finesse of 150 000 and a length of 51 cm. Higher-frequency sidebands, generated at 305 MHz and matched to the free spectral range of the cavity, are used to produce the NICE-OHMS signal [4]. For further noise reduction, a low-frequency (405 Hz) wavelength dither is applied on one of the cavity mirrors. For the demodulation steps and registration of the signal, an advanced high-frequency lock-in detector (Zurich Instruments, HF2LI) is utilized.

The frequency of the external-cavity diode laser (ECDL) is calibrated *via* a fiber link to an in-house metrology station, consisting of a frequency-comb laser, a Cs clock, and a device receiving signals from the global positioning system (GPS). Through this metrology station, long-term stabilization is ensured for the beatnote of the cavity-locked laser by a slow feedback on the cavity piezo for controlled acquisition and frequency scans. This construction allows the achievement of a frequency precision below 1 kHz.

Since the generic signal of NICE-OHMS is dispersive, the additional wavelength dither on the cavity produces a symmetric line shape, resembling the second derivative of a Voigt profile if 1f

Optics EXPRESS

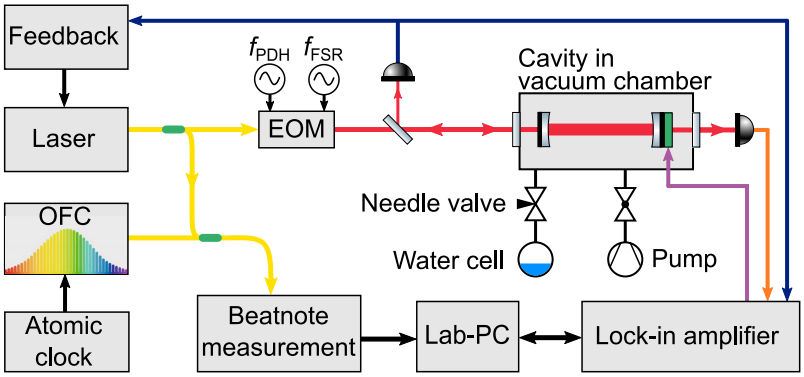

Fig. 1. Schematic layout of the NICE-OHMS setup employed during this study. NICE-OHMS = noise-immune cavity-enhanced optical-heterodyne-molecular spectroscopy, OFC = optical frequency comb, EOM = electro-optic modulator, FSR = free spectral range of the cavity, and PDH = Pound–Drever–Hall locking.

demodulation is employed. For the present measurement campaign, the relative absorption of the Lamb-dip features is typically on the order of 10^{-11} cm^{-1}, while the resonance widths are approximately 400–800 kHz (full width at half maximum, FWHM). In this study, intracavity powers of 5–100 W are utilized. Low powers are typically used to probe strong transitions, for which the Lamb-dips may suffer from power broadening. In a previous study [13], it was observed that strong lines eventually exhibit doubled Lamb-dip features at high power. This phenomenon, specifically associated with the NICE-OHMS detection technique, is avoided here to not confuse the new features observed in this study with doubled Lamb dips.

The wavenumber coverage of our NICE-OHMS spectrometer in its current setup is 7000–7350 cm^{-1}, limited by the tuning range of the ECDL, the highly-reflective cavity mirrors, as well as the transmission properties of certain electro-optical components. The accessible window of dipole moments, represented by the Einstein-A coefficients, falls in the interval of 10^{-4}–10^{2} s^{-1}. Combined with the population distribution at the measurement temperature (T = 293 K), the allowed range of intensities corresponds to 10^{-26}–10^{-20} cm molecule^{-1}.

2.2. Notation

In this study, rovibrational states of water isotopologues are labelled as $(v_1\ v_2\ v_3)J_{K_a,K_c}$, where $(v_1\ v_2\ v_3)$ is the vibrational assignment based on the normal-mode picture, while J_{K_a,K_c} stands for the standard asymmetric-top rotational quantum numbers [18]. The v_1, v_2, and v_3 quantum numbers correspond, respectively, to (a) the symmetric stretch, bend, and antisymmetric stretch normal modes for $H_2{}^{16}O$ and $H_2{}^{18}O$, and (b) the O–D stretch, bend, and O–H stretch fundamentals for $HD^{16}O$ and $HD^{18}O$. A rovibrational transition is denoted as $(v'_1\ v'_2\ v'_3)J'_{K'_a,K'_c} \leftarrow (v''_1\ v''_2\ v''_3)J''_{K''_a,K''_c}$, where $'$ and $''$ distinguish between the upper and lower states, respectively.

The parity of a $(v_1\ v_2\ v_3)J_{K_a,K_c}$ state is even/odd (e/o or +/−) if K_c is even/odd. As the states $(v_1\ v_2\ v_3)J_{K_a,\dot{K}_c}$ and $(v_1\ v_2\ v_3)J_{K_a,\ddot{K}_c}$ with $\left|\dot{K}_c - \ddot{K}_c\right| = 1$ practically differ only in their parity, they form what we call a *parity pair*. This parity pair is denoted as $(v_1\ v_2\ v_3)J_{K_a,\dot{K}_c/\ddot{K}_c}$ if $\dot{K}_c$ belongs to the higher-energy state. The energy difference of a parity pair is hereinafter called K_c *splitting*. Clearly, the parity pairs of H_2O isotopologues are *ortho–para* nuclear-spin-isomer pairs. If U_1/U_2 and L_1/L_2 are parity pairs, then the transition doublet $(U_1 \leftarrow L_1, U_2 \leftarrow L_2)$ is named a *parity doublet*. By convention, $(v'_1\ v'_2\ v'_3)J'_{K'_a,\dot{K}'_c/\ddot{K}'_c} \leftarrow (v''_1\ v''_2\ v''_3)J''_{K''_a,\dot{K}''_c/\ddot{K}''_c}$ indicates a parity doublet

Optics EXPRESS

whose higher- and lower-frequency lines are assigned as $(v_1' \, v_2' \, v_3')J'_{K_a',\dot{K}_c'} \leftarrow (v_1'' \, v_2'' \, v_3'')J''_{K_a'',\dot{K}_c''}$ and $(v_1' \, v_2' \, v_3')J'_{K_a',\dot{K}_c'} \leftarrow (v_1'' \, v_2'' \, v_3'')J''_{K_a'',\dot{K}_c''}$, respectively.

2.3. *Effective Hamiltonian and variational computations*

There are several investigations [19,23–28] which have helped to determine the empirical energy-level structure of $HD^{16}O$ in its ground vibrational state, $(v_1 \, v_2 \, v_3) = (0\,0\,0)$. These studies involved more than 600 pure rotational Lamb-dip lines, often with resolved hyperfine structure. Based on these transitions, a global fit was performed in Ref. 19, yielding effective-Hamiltonian (EH) energies for the (0 0 0) rotational states with an accuracy of 10^{-8}–10^{-6} cm^{-1}.

The empirical energies available for the (0 0 2) rotational states are considerably less accurate, they are on the order of 10^{-3} cm^{-1}, as typically obtained from Doppler-limited rovibrational spectroscopy [28]. As shown in Refs. 9,10 and 13, small (<0.01 cm^{-1}) energy differences can be estimated much more accurately than 10^{-3} cm^{-1} *via* first-principles nuclear-motion computations, provided that the underlying energy levels share the same vibrational state and J value. Therefore, such computations have been carried out, up to $J = 8$, for $HD^{16}O$ and $HD^{18}O$ with the GENIUSH (**GE**neral rovibrational code with **N**umerical, **I**nternal-coordinate, **U**ser-**S**pecified **H**amiltonians) code [29–31], using the potential energy surface of Ref. 32 and a sufficiently large vibrational basis set (as usual, the rotational basis is complete).

The computed K_c splittings of $HD^{16}O$ and $HD^{18}O$, as well as the EH-based estimates of Ref. 19, are given fully in Dataset 1 [33] and partly in Fig. 2. As apparent from panels (a) and (b) of Fig. 2, the variational K_c splittings of $HD^{16}O$ follow a monotonically decreasing trend as a function of K_a, for each J value, in the (0 0 0) and (0 0 2) vibrational states, respectively. It must be noted that the computed K_c splittings are in a remarkable agreement with their EH-based analogues in the (0 0 0) state: their deviations are on the order of 0.1–5 % relative to the actual K_c splitting values. In absolute terms, the discrepancies are well within 1 MHz when both J and K_a are larger than 2, showing the high absolute accuracy of the computed K_c splittings, especially at higher J and K_a values.

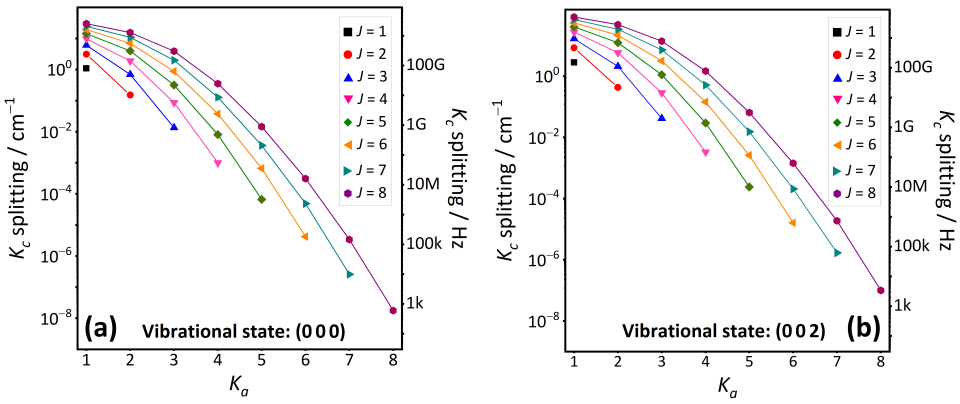

Fig. 2. Variationally computed K_c splittings of the $HD^{16}O$ molecule up to $J = 8$. Panels (a) and (b) correspond to the (0 0 0) and (0 0 2) vibrational states, respectively. The K_c splittings are plotted, with various colors, for each J value separately and connected with solid lines (the exceptions are the single $J = 1$ points). The K_c splittings are given both in cm^{-1} (left vertical axes) and in Hz (right vertical axes).

Optics EXPRESS

3. Experimental results

3.1. Regular and perturbed Lamb-dip profiles

During the present NICE-OHMS study, Lamb dips were measured for more than 100 rovibrational transitions of $HD^{16}O$. A number of spectral lines recorded and analyzed exhibit a typical Lamb-dip profile, similar to the cases of the symmetric water isotopologues $H_2{}^{16}O$ [9,13] and $H_2{}^{18}O$ [10]. Figure 3 displays four symmetric Lamb dips of different strength for four transitions, exemplifying, at the same time, the remarkable signal-to-noise ratio obtained. In panels (b) and (d) of Fig. 3, some additional broadening is clearly visible, which is an evident proof of power broadening.

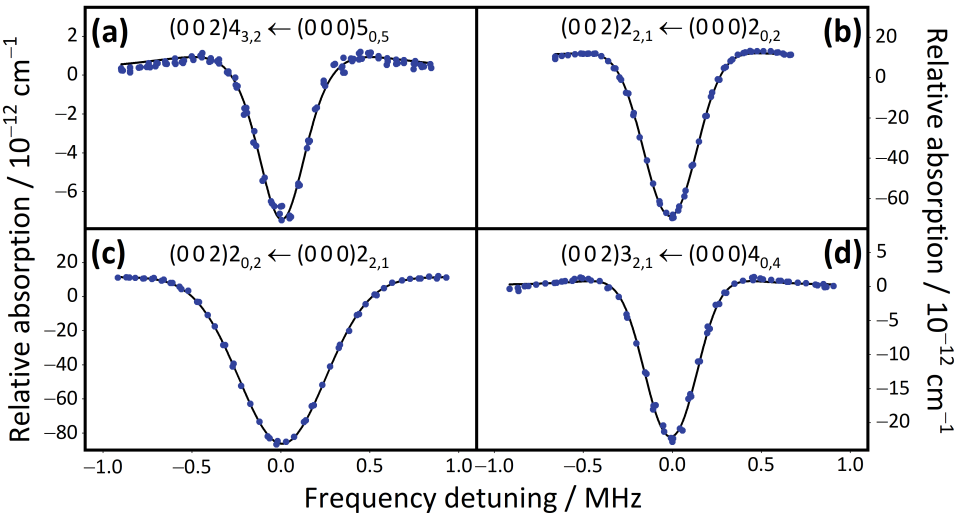

Fig. 3. Typical symmetric Lamb dips observed for a few transitions of $HD^{16}O$. The relative absorption strengths are indicated along the vertical axes. The spectra are plotted in the same detuning interval, showing significant differences in the line widths. The line centers, corresponding to zero detunings and given in kHz, are the following: 218 999 237 631 [panel (a)], 218 996 338 105 [panel (b)], 215 464 997 071 [panel (c)], and 217 318 701 228 [panel (d)].

For transitions with $\max(K'_a, K''_a)>3$, asymmetric Lamb-dip profiles have been found. To improve our understanding about the origin of this asymmetry, Lamb dips of a selected transition doublet, involving the (0 0 0)$4_{4,0/1}$ and (0 0 2)$4_{3,1/2}$ parity pairs, were recorded for four water isotopologues: $HD^{16}O$, $HD^{18}O$, $H_2{}^{16}O$, and $H_2{}^{18}O$. The experimental results of Fig. 4 show that asymmetry occurs only in the spectra of the two HDO species. This clearly suggests that the spectral distortion is due to the H→D substitution and must be related to the different nuclear-spin symmetry of H_2O and HDO.

For higher J and K_a values, the Lamb-dip profiles become gradually more complex, leading to multi-component spectral structures. Figure 5 gives an example for a parity doublet, (0 0 2)$7_{6,1/2}$ ← (0 0 0)$6_{6,0/1}$, yielding very similar multi-component features for $HD^{16}O$ and $HD^{18}O$. In $H_2{}^{16}O$ and $H_2{}^{18}O$, this doublet, consisting of strongly forbidden *ortho-para* transitions, is not measured. Since the variationally computed line separations are 6.07 and 6.61 MHz for $HD^{16}O$ and $HD^{18}O$, respectively, the resonances at detunings of ±3.0 ($HD^{16}O$) and ±3.3 MHz ($HD^{18}O$) are the main transition centers. Our variational computations also suggest that (0 0 2)$7_{6,2}$ ← (0 0 0)$6_{6,1}$ is the lower-frequency line for both species. While the additional resonances are not analyzed in this extreme case, a semi-quantitative approach will be presented

Optics EXPRESS

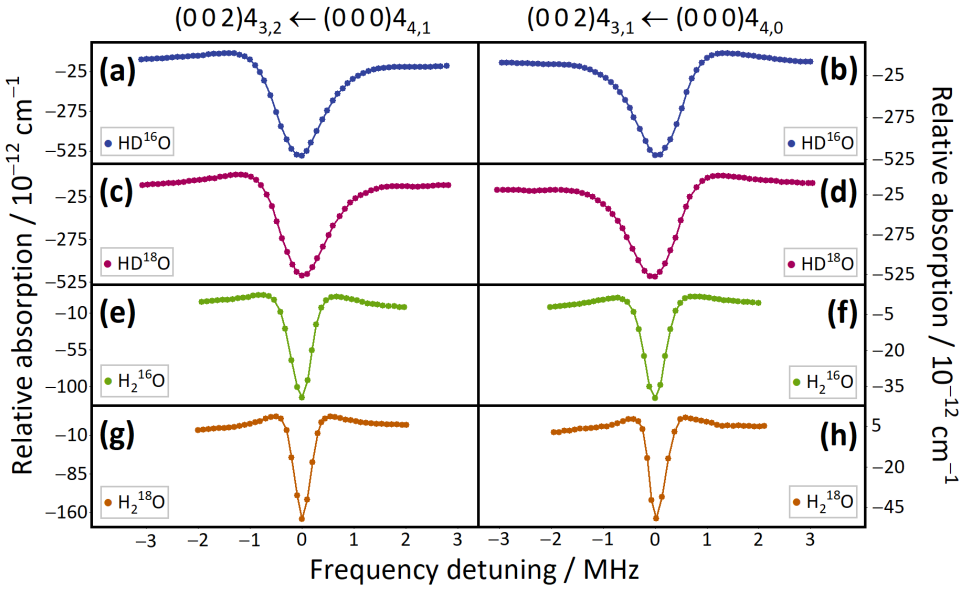

Fig. 4. Lamb dips for a well-isolated parity doublet of various water isotopologues. Note the asymmetric broadening for the $HD^{16}O$ and $HD^{18}O$ isotopologues, in contrast to the fully symmetric resonances of the $H_2{}^{16}O$ and $H_2{}^{18}O$ species. The line centers, corresponding to zero detunings and given in kHz, are the following: 213 591 493 210 [panel (a)], 213 600 053 170 [panel (b)], 213 012 275 678 [panel (c)], 213 021 144 460 [panel (d)], 219 363 999 176 [panel (e)], 219 416 311 674 [panel (f)], 218 657 009 781 [panel (g)], and 218 712 072 101 [panel (h)].

in Sec. 4 to explain the substructures of various multi-component $HD^{16}O$ lines observed during this study.

To prove that the multi-component Lamb-dip profiles of HDO are not due to the special features of the NICE-OHMS method (*i.e.*, the frequency sidebands shifted by ±305 MHz from the carrier frequency), the saturation spectrum of the $HD^{16}O$ parity doublet depicted in Fig. 5(b) was also recorded with the wavelength-modulated CEAS (WM-CEAS) technique [20]. To obtain the best resemblance with the dispersive 1*f* NICE-OHMS signal, the WM-CEAS spectrum, resulting from direct absorption, was recorded at 2*f* demodulation. The WM-CEAS technique yielded a similarly complex Lamb-dip profile, see Fig. 5(c), albeit at lower signal-to-noise ratio. From this observation, one can conclude that these perturbations can be attributed to the use of saturation spectroscopy in general, and not to the special characteristics of the NICE-OHMS method.

3.2. *Assessment of line-center uncertainties*

A list of selected $HD^{16}O$ transitions, whose frequencies could be extracted unambiguously, are presented in Table 1. The majority of the lines listed correspond to those cases for which single, symmetric Lamb dips were measured. For a few transitions, with frequencies set in bold face in Table 1, significant Lamb-dip asymmetry was observed. It must be stressed that no individual uncertainties are reported in Table 1, see the upcoming paragraphs for a detailed reasoning.

Under ideal circumstances, the uncertainty of the HDO line centers determined during this study should be similar to those obtained in previous studies on $H_2{}^{16}O$ [9,13] and $H_2{}^{18}O$ [10]. Beyond the statistical uncertainties (2–5 kHz), there is a minor systematic effect due to frequency calibration (1 kHz). To ascertain the magnitude of pressure shifts, five $HD^{16}O$ transitions were studied over a set of pressure values. This analysis yielded an estimate of 4–8 kHz for the

Optics EXPRESS

Table 1. A list of selected transitions observed during the present study for $HD^{16}O$.[a]

#	Assignment	Frequency/kHz	#	Assignment	Frequency/kHz	#	Assignment	Frequency/kHz
1	$4_{3,2} \leftarrow 5_{4,1}$	**211 255 218 752**	34	$4_{2,3} \leftarrow 5_{1,4}$	215 630 896 331	67	$1_{0,1} \leftarrow 0_{0,0}$	217 824 645 006
2	$4_{3,1} \leftarrow 5_{4,2}$	**211 264 320 484**	35	$2_{2,1} \leftarrow 3_{2,2}$	215 722 128 619	68	$2_{0,2} \leftarrow 1_{1,1}$	217 836 884 655
3	$2_{0,2} \leftarrow 3_{3,1}$	211 744 649 702	36	$2_{1,2} \leftarrow 2_{2,1}$	215 761 267 929	69	$2_{1,1} \leftarrow 2_{0,2}$	217 896 321 707
4	$2_{1,2} \leftarrow 3_{3,1}$	212 040 920 563	37	$4_{1,3} \leftarrow 3_{3,0}$	215 763 215 736	70	$4_{1,3} \leftarrow 3_{2,2}$	218 091 469 253
5	$3_{2,2} \leftarrow 4_{3,1}$	212 893 380 771	38	$2_{0,2} \leftarrow 3_{0,3}$	215 992 511 353	71	$2_{1,2} \leftarrow 1_{1,1}$	218 133 155 517
6	$3_{2,1} \leftarrow 4_{3,2}$	212 961 789 398	39	$2_{1,2} \leftarrow 3_{1,3}$	216 017 150 744	72	$1_{1,1} \leftarrow 0_{0,0}$	218 192 618 433
7	$3_{0,3} \leftarrow 3_{3,0}$	213 071 606 762	40	$3_{1,2} \leftarrow 3_{2,1}$	216 067 168 586	73	$2_{0,2} \leftarrow 1_{0,1}$	218 265 598 825
8	$2_{2,1} \leftarrow 3_{3,0}$	213 393 875 116	41	$5_{1,4} \leftarrow 5_{2,3}$	216 069 120 601	74	$5_{2,3} \leftarrow 5_{1,4}$	218 267 454 989
9	$2_{2,0} \leftarrow 3_{3,1}$	213 407 644 235	42	$4_{1,3} \leftarrow 4_{2,2}$	216 099 435 929	75	$2_{1,1} \leftarrow 1_{1,0}$	218 306 340 106
10	$3_{0,3} \leftarrow 4_{2,2}$	213 407 826 955	43	$3_{2,2} \leftarrow 4_{1,3}$	216 271 857 536	76	$3_{0,3} \leftarrow 2_{1,2}$	218 315 704 705
11	$4_{3,2} \leftarrow 4_{4,1}$	**213 591 493 161**	44	$2_{1,2} \leftarrow 3_{0,3}$	216 288 782 215	77	$5_{1,4} \leftarrow 5_{1,5}$	218 411 396 736
12	$4_{3,1} \leftarrow 4_{4,0}$	**213 600 053 221**	45	$5_{1,4} \leftarrow 4_{3,1}$	216 318 468 066	78	$5_{1,4} \leftarrow 5_{0,5}$	218 528 878 204
13	$4_{1,3} \leftarrow 4_{3,2}$	213 891 431 851	46	$4_{4,1} \leftarrow 4_{4,0}$	**216 390 846 543**	79	$3_{2,1} \leftarrow 2_{2,0}$	218 544 467 143
14	$4_{1,3} \leftarrow 5_{2,4}$	213 946 914 959	47	$4_{4,0} \leftarrow 4_{4,1}$	**216 391 002 295**	80	$4_{3,2} \leftarrow 3_{3,1}$	218 667 138 981
15	$5_{1,4} \leftarrow 5_{3,3}$	213 980 435 634	48	$1_{1,1} \leftarrow 2_{1,2}$	216 450 017 996	81	$5_{4,2} \leftarrow 4_{4,1}$	**218 707 043 907**
16	$3_{1,2} \leftarrow 4_{2,3}$	214 269 098 930	49	$4_{3,2} \leftarrow 5_{2,3}$	216 539 480 025	82	$5_{4,1} \leftarrow 4_{4,0}$	**218 707 875 972**
17	$4_{3,1} \leftarrow 5_{3,2}$	214 437 102 684	50	$2_{0,2} \leftarrow 2_{1,1}$	216 746 361 259	83	$3_{2,2} \leftarrow 3_{1,3}$	218 747 922 447
18	$4_{3,2} \leftarrow 5_{3,3}$	214 450 795 065	51	$5_{3,3} \leftarrow 5_{3,2}$	216 751 348 607	84	$3_{1,3} \leftarrow 2_{0,2}$	218 885 916 082
19	$1_{0,1} \leftarrow 2_{2,0}$	214 548 840 462	52	$3_{1,3} \leftarrow 3_{1,2}$	216 778 728 414	85	$2_{2,1} \leftarrow 2_{0,2}$	218 996 338 105
20	$4_{2,3} \leftarrow 4_{3,2}$	214 723 994 038	53	$3_{0,3} \leftarrow 2_{2,0}$	216 782 500 605	86	$4_{3,2} \leftarrow 5_{0,5}$	218 999 237 631
21	$3_{2,2} \leftarrow 3_{3,1}$	214 771 692 247	54	$4_{3,1} \leftarrow 4_{3,2}$	216 803 145 429	87	$5_{2,4} \leftarrow 5_{1,5}$	219 074 884 146
22	$4_{2,3} \leftarrow 5_{2,4}$	214 779 477 149	55	$2_{2,1} \leftarrow 3_{1,2}$	216 889 150 425	88	$6_{4,3} \leftarrow 5_{4,2}$	**219 156 438 857**
23	$3_{2,1} \leftarrow 3_{3,0}$	214 833 573 282	56	$5_{2,4} \leftarrow 4_{3,1}$	216 981 955 478	89	$6_{4,2} \leftarrow 5_{4,1}$	**219 160 293 903**
24	$1_{1,1} \leftarrow 2_{2,0}$	214 916 813 889	57	$3_{1,3} \leftarrow 2_{2,0}$	216 994 346 943	90	$5_{3,3} \leftarrow 5_{2,4}$	219 172 874 489
25	$6_{4,3} \leftarrow 5_{5,0}$	**215 087 471 023**	58	$2_{1,2} \leftarrow 2_{1,1}$	217 042 632 138	91	$5_{2,4} \leftarrow 4_{2,3}$	219 339 389 708
26	$6_{4,2} \leftarrow 5_{5,1}$	**215 091 816 331**	59	$3_{2,2} \leftarrow 3_{2,1}$	217 048 884 659	92	$2_{2,1} \leftarrow 1_{1,0}$	219 406 356 492
27	$3_{2,2} \leftarrow 4_{2,3}$	215 250 815 000	60	$2_{2,0} \leftarrow 2_{2,1}$	217 127 991 606	93	$2_{2,0} \leftarrow 1_{1,1}$	219 499 879 187
28	$3_{1,2} \leftarrow 4_{1,3}$	215 290 141 481	61	$3_{2,1} \leftarrow 4_{1,4}$	217 132 050 435	94	$4_{4,0} \leftarrow 4_{3,1}$	**219 588 336 492**
29	$3_{0,3} \leftarrow 3_{2,2}$	215 399 860 259	62	$3_{2,1} \leftarrow 4_{0,4}$	217 318 701 228	95	$4_{4,1} \leftarrow 4_{3,2}$	**219 593 939 070**
30	$2_{0,2} \leftarrow 2_{2,1}$	215 464 997 071	63	$5_{2,3} \leftarrow 4_{3,2}$	217 360 552 700	96	$2_{2,0} \leftarrow 1_{0,1}$	219 928 593 355
31	$3_{0,3} \leftarrow 4_{0,4}$	215 556 734 694	64	$5_{2,3} \leftarrow 5_{2,4}$	217 416 035 798	97	$3_{2,1} \leftarrow 2_{1,2}$	220 077 671 240
32	$3_{1,3} \leftarrow 4_{1,4}$	215 581 930 240	65	$3_{1,2} \leftarrow 2_{2,1}$	217 510 323 548	98	$4_{2,3} \leftarrow 3_{1,2}$	220 091 053 247
33	$3_{1,3} \leftarrow 3_{2,2}$	215 611 706 593	66	$3_{1,2} \leftarrow 3_{1,3}$	217 766 206 377			

[a]The vibrational states $(v'_1\ v'_2\ v'_3) = (0\,0\,2)$ and $(v''_1\ v''_2\ v''_3) = (0\,0\,0)$ are not indicated in the rovibrational assignments. The plain frequencies are expected to be accurate to 100 kHz or better. The bold values, corresponding to transitions with significant spectral asymmetry around their Lamb dips, may have larger uncertainties (presumably less than 1 MHz). The lines of this table are given as a text file in Dataset 2 [34].

Optics EXPRESS

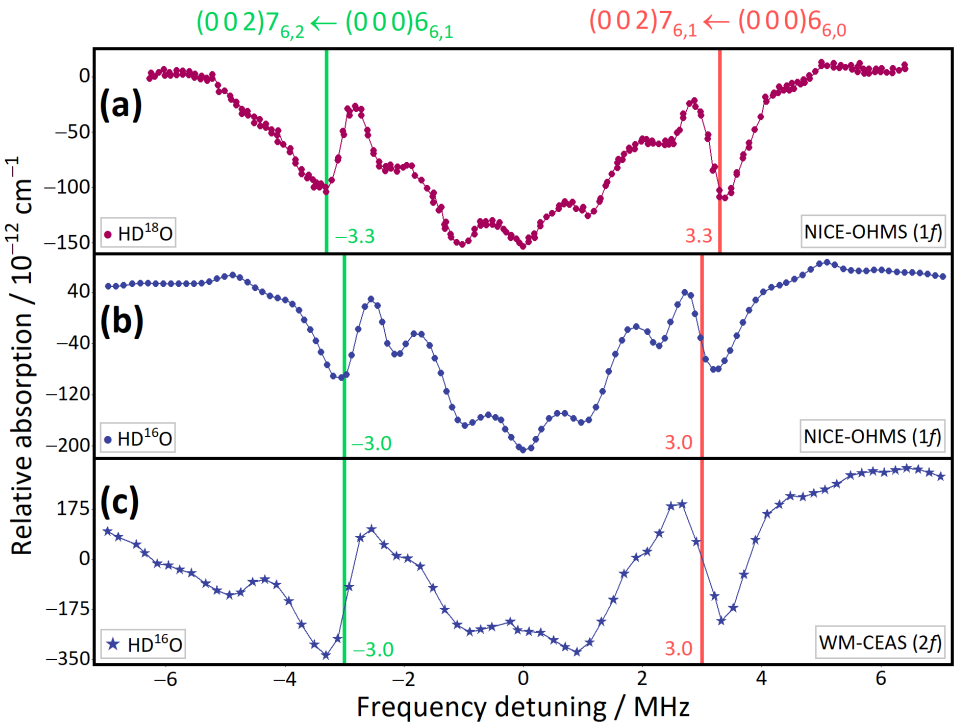

Fig. 5. Multi-component saturation spectra detected for a parity doublet of HDO. Panels (a) and (b) show the recordings for the (0 0 2)$7_{6,1/2}$ ← (0 0 0)$6_{6,0/1}$ doublet of $HD^{18}O$ and $HD^{16}O$, respectively. In both spectra, the two outermost dips represent the main transition centers. The colors of the vertical bars are matched with the rovibrational assignments. Note that these transitions are forbidden in $H_2^{16}O$ and $H_2^{18}O$ due to *ortho-para* selection rules. Panel (c) exhibits the spectrum observed with the wavelength-modulated CEAS (WM-CEAS) technique. The symbols 1*f* and 2*f* denote the demodulation technique employed in the measurements. The detuning scale is relative to the absolute frequencies: 217 816 033 008 kHz for panel (a) and 218 444 739 748 kHz for panels (b) and (c).

pressure-shift uncertainties of the remaining transitions measured at a pressure of 0.1–0.2 Pa. Taking all these uncertainty factors into account, the overall precision of the Lamb-dip centers reported in Table 1 is in the range of 2–20 kHz.

As noted in Sec. 3.1, those HDO lines with max (K_a', K_a'')>3 produce distorted spectra even when saturation-spectroscopy techniques other than NICE-OHMS are employed. Thus, the possible frequency shifts due to the asymmetry effects observed cannot be uncovered through a direct comparison with results of independent nonlinear spectroscopic methods. For this reason, an indirect procedure is chosen to provide at least a partial assessment for the accuracy of our NICE-OHMS lines. This approach involves the comparison of the experimental K_c splittings, related to the ground vibrational state and determined by our NICE-OHMS transition dataset, with their counterparts deduced from the pure rotational EH model of Ref. 19.

Numerical values of the K_c splittings, together with the frequency combinations employed, are presented in Table 2. Table 2 shows that there are a number of deviations larger than our experimental precision, 2–20 kHz, but all deviations remain smaller than 0.5 MHz. (Note that in our earlier study [9] on $H_2^{16}O$, no systematic deviations were observed during the EH analysis of the pure rotational energy levels.) When plotting the unsigned K_c-splitting deviations as a function of the EH-based K_c splittings (see Fig. 6), it can be observed that these deviations are the

Optics EXPRESS

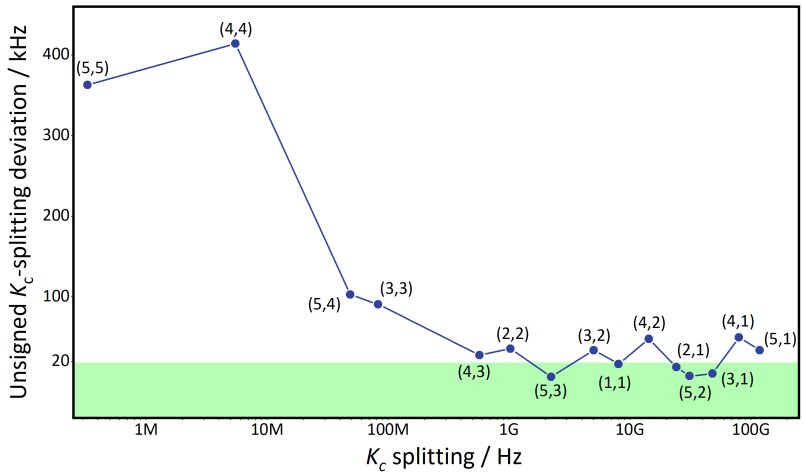

Fig. 6. Unsigned K_c-splitting deviations as a function of the individual K_c-splittings. The K_c splittings and the unsigned deviations are taken from the third and fourth columns of Table 2, respectively. The data point pertaining to the $(0\,0\,0)J_{K_a,J-K_a/J-K_a+1}$ parity pair is labelled as (J, K_a). The horizontal green strip at 20 kHz represents the typical experimental reproducibility of the NICE-OHMS lines.

Table 2. Experimental and effective-Hamiltonian K_c splittings of $HD^{16}O$ up to $J = 5$.[a]

Parity pair	$\Delta^{\mathrm{expt}}(K_c)$/kHz	$\Delta^{\mathrm{EH}}(K_c)$/kHz	δ/kHz	Frequency combination
$1_{1,0/1}$	80 578 326	80 578 309	17	$F_{68} - F_{30} + F_{65} - F_{40} - F_0 + F_{32} - F_{84} + F_{85} - F_{92}$
$2_{1,1/2}$	241 561 624	241 561 638	–13	$F_{97} - F_{61} + F_0 + F_{40} - F_{65} + F_{36} - F_{58}$
$2_{2,0/1}$	10 278 268	10 278 233	36	$F_{65} - F_{40} - F_0 + F_{32} - F_{57}$
$3_{1,2/3}$	481 779 626	481 779 631	–5	$F_{66} - F_{40} - F_0 + F_{32} - F_{52}$
$3_{2,1/2}$	50 236 344	50 236 309	34	$F_{33} - F_{32} + F_0$
$3_{3,0/1}$	824 754	824 663	91	$F_{21} - F_{27} + F_{16} - F_{40} - F_0 + F_{61} - F_{23}$
$4_{1,3/4}$	797 487 096	797 487 146	–50	$F_0 + F_{40} - F_{28}$
$4_{2,2/3}$	143 727 314	143 727 265	48	$F_{16} - F_{40} - F_0 + F_{61} - F_{23} + F_{37} - F_{42}$
$4_{3,1/2}$	5 702 838	5 702 811	28	$F_6 - F_{61} + F_0 + F_{40} - F_{16} + F_{27} - F_5$
$4_{4,0/1}$	55 034	54 619	414	$F_{11} - F_{18} + F_{15} - F_{45} + F_5 - F_{27} + F_{16} - F_{40} - F_0 + F_{61} - F_6 + F_{54} - F_{12}$
$5_{1,4/5}$	1 180 323 536	1 180 323 570	–34	$F_{87} - F_{91} + F_{16} - F_{40} - F_0 + F_{61} - F_6 + F_{20} - F_{34}$
$5_{2,3/4}$	310 533 410	310 533 412	–2	$F_{14} - F_{37} + F_{23} - F_{61} + F_0 + F_{40} - F_{16} + F_{27} - F_5 + F_{45} - F_{41}$
$5_{3,2/3}$	22 307 474	22 307 476	–1	$F_{15} - F_{45} + F_5 - F_{27} + F_{16} - F_{40} - F_0 + F_{61} - F_6 + F_{54} - F_{17}$
$5_{4,1/2}$	486 638	486 536	103	$F_2 - F_{54} + F_6 - F_{61} + F_0 + F_{40} - F_{16} + F_{27} - F_5 + F_{45} - F_{15} + F_{18} - F_1$
$5_{5,0/1}$	3 624	3 260	363	$F_{26} - F_{89} + F_1 - F_{18} + F_{15} - F_{45} + F_5 - F_{27} + F_{16} - F_{40} - F_0 + F_{61} - F_6 + F_{54} - F_2 + F_{88} - F_{25}$

[a]The first column contains the $J_{K_a,J-K_a/J-K_a+1}$ assignment of parity pairs, without indicating their vibrational state, (0 0 0). The last column specifies which frequency combinations have been taken to obtain the experimental K_c splittings, $\Delta^{\mathrm{expt}}(K_c)$. Symbol F_i (i>0) corresponds to the frequency of the line listed with serial number i in Table 1, while F_0 = 20 459 990.5 ± 0.3 kHz is the extremely accurate frequency of the $(0\,0\,0)3_{2,1} \leftarrow (0\,0\,0)4_{1,4}$ microwave transition taken from Ref. 27. The effective-Hamiltonian (EH) splittings, $\Delta^{\mathrm{EH}}(K_c)$, are derived from the EH model of Ref. 19. The fourth column includes the signed K_c-splitting deviations, defined as $\delta = \Delta^{\mathrm{expt}}(K_c) - \Delta^{\mathrm{EH}}(K_c)$.

largest where the K_c splittings are the smallest. Although there is no asymmetry in the Lamb dips used to derive the K_c splitting of the $(0\,0\,0)3_{3,0/1}$ pair, a relatively large deviation (91 kHz) can be seen for $(J, K_a) = (3, 3)$. Apparently, the centers of symmetric Lamb dips may also become

Optics EXPRESS

shifted in our nonlinear spectroscopic experiments. Based on the fourth column of Table 2, the underlying transitions may have uncertainties on the order of 100 kHz for $\max(K'_a, K''_a) \leq 3$ and even significantly higher (probably less than 1 MHz) for $\max(K'_a, K''_a)$>3.

4. Phenomenological Lamb-dip-profile analysis

As mentioned in Sec. 3.1, during this study significant perturbations have been observed for the Lamb dips of $HD^{16}O$ and $HD^{18}O$ lines. For a parity doublet of the two HDO species, see panels (a)–(d) of Fig. 4, highly asymmetric Lamb-dip shapes were identified, which are similar to the typical profiles resulting from an (optical) AC-Stark effect [35,36]. In this section, an attempt is made to find a semi-quantitative explanation for the complex Lamb dips of HDO.

4.1. General framework: Stark-induced parity-pair mixing and cross-overs

We postulate that the cause of the significant perturbations in the Lamb dips of HDO originate in an interaction (mixing) of parity pairs. Since intramolecular perturbations occur only between quantum states of the same parity, the interaction mechanism of parity pairs must be related to an external cause. Such cause can be found in the intense laser field within the cavity, inducing an AC-Stark effect [37,38] between the two states of a parity pair. An argument supporting our hypothesis stems from perturbation theory, underpinning that interactions become larger when the interacting states, that is the two states of a parity pair in our case, are in proximity. The fact that spectral perturbations do not occur for H_2O, where parity pairs correspond to non-interacting *ortho-para* nuclear-spin-isomer pairs, further supports our assumption on parity-pair mixing in HDO.

Figure 7(a) displays how extra resonances can occur in the presence of close-lying parity pairs. The lines with frequencies a_1 and a_2 are dipole-allowed (a-type) transitions, following dipole-selection rules. With the decrease of the K_c splittings, the AC-Stark mixing of parity pairs becomes more significant and thus makes the dipole-forbidden (parity-preserving, f-type) lines, with frequencies $f_1 = a_2 - \Delta_U(K_c)$ and $f_2 = a_1 + \Delta_U(K_c)$ [see Fig. 7(a) and Supplement 1 [39] Sec. S1], quantum mechanically allowed in an intensity-borrowing process. Although the f-type transitions coincide with quadrupole lines on the frequency scale, they are are much stronger than generic quadrupole transitions. All the lines of Fig. 7(a) can be detected in saturation spectroscopy, based on the excitation of velocity components with $v_z = 0$, where v_z is the molecular velocity along the intra-cavity laser-beam propagation.

As explained in Ref. [40], the saturation conditions can induce additional lines, called cross-over (c-type) resonances, due to probing velocity classes different from those leading to regular Lamb dips. If two transition frequencies are close to each other in a V/Λ scheme [see Fig. 7(b)], a c-type resonance appears at the average of the two frequencies. In fact, such a c-type resonance is delivered by the interaction of the counter-propagating carrier beams with Doppler-shifted $v_z \neq 0$ velocity classes. Therefore, cross-overs are only produced when the Doppler profiles overlap for the two transitions of a V/Λ scheme. As obvious from Fig. 7(b), these c-type resonances can be treated as artificial transitions $V_U \leftarrow l$ and $u \leftarrow V_L$, where u/l denotes an arbitrary upper/lower state and V_X is a virtual state at halfway between the two states of the $X = (X_1, X_2)$ pair. Cross-over features were previously observed in (hyper)fine spectra [41,–43] and also in the Stark-perturbed spectrum of neon [44].

In our case, the c-type resonances are connected to parity pairs, as illustrated in Fig. 7(c). Considering all possible V and Λ schemes between triplets (L_1, V_L, L_2) and (U_1, V_U, U_2), five distinct cross-overs with frequencies c_0, c_1, c_2, C_1, and C_2 can be specified. The c_0 line, which pertains to the V scheme of (C_1, C_2) [and also to the Λ scheme of (c_1, c_2)], can be viewed as a higher-order cross-over resonance. In total, the nine near-infrared resonances form a nonuplet, as shown in Fig. 7(c).

Optics EXPRESS

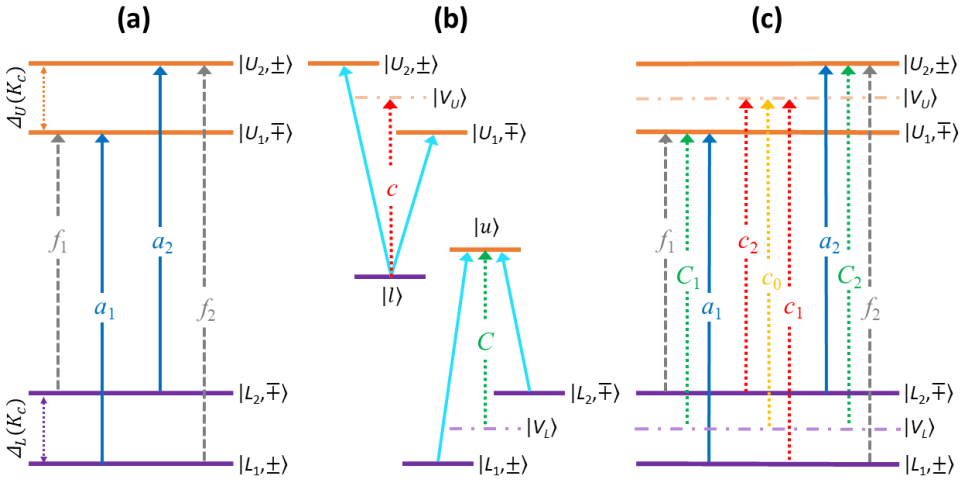

Fig. 7. Illustration of the extra resonances observed during the present study. The panels of this figure show (a) the transitions produced by parity-pair mixing, (b) the cross-over resonances in V (left) and Λ (right) schemes, and (c) the nonuplet formed by the lines of panel (a) and their cross-overs. In the V (Λ) scheme, the two general (cyan) transitions share a common lower (upper) state. The parity pairs $U = (U_1, U_2)$ and $L = (L_1, L_2)$ belong to different vibrational states. The parity of a state is indicated within the ket symbol. The kets $|l\rangle$ and $|u\rangle$ of panel (b) stand for arbitrary lower and upper states, respectively. $\Delta_X(K_c)$ and V_X are the K_c splitting and the (halfway) virtual state of $X = (X_1, X_2)$, respectively. The arrows in solid blue, dashed gray, and dotted red/green/yellow represent dipole-allowed (a-type), dipole-forbidden (f-type), and cross-over (c-type) lines, respectively. The labels on the arrows designate the resonance frequencies. Although L_1 and U_1 are chosen here to have opposite parity, the reverse case can also be realized (see Supplement 1 [39] Fig. S1). Both cases occurred during this study. The possible frequency orderings of the nine lines are presented in Supplement 1 [39] Table S1. The line frequencies relative to c_0 can be expressed as a combination of the two splitting values (see Supplement 1 [39] Sec. S1).

The intensities of the extra (f- and c-type) lines do not straightforwardly result from Wigner-6J symbols, as is the case for hyperfine transitions. These intensities can be obtained from the numerical solution of the optical Bloch equations by integrating signals over the entire velocity distribution within the Doppler profile, as was shown in a recent study on HD [17]. As a result, the extra lines may acquire positive or negative excess intensity and thus generate Lamb dips or Lamb peaks, respectively [17,45]. In some cases, the c-type lines may be more intense than the a-type transitions.

4.2. Assignment of complex Lamb-dip spectra of $HD^{16}O$

Relying on the EH-based and variational K_c splittings of the (0 0 0) and (0 0 2) vibrational states, respectively, our semi-quantitative approach is followed in this subsection to understand the relative positions of the observed extra lines at a sub-MHz level of accuracy, but no explanation is provided for the resonance intensities. Below, some typical multi-component Lamb-dip spectra of $HD^{16}O$ are documented and analyzed. Furthermore, a complex saturation spectrum is presented around the $(0\,0\,2)3_{2,1/2} \leftarrow (0\,0\,0)3_{3,0/1}$ doublet (see Supplement 1 [39] Sec. S2), where the a-type lines are characterized with well-isolated symmetric Lamb-dip profiles. This spectrum (see Fig. S2) shows two f-type resonances shifted from the a-type lines by ±824.7 MHz, corresponding to the K_c splitting of the $(0\,0\,0)3_{3,0/1}$ parity pair.

Optics EXPRESS

4.2.1. $(0\,0\,2)4_{3,1/2} \leftarrow (0\,0\,0)4_{4,0/1}$ doublet

As discussed in Sec. 3.1, highly asymmetric Lamb-dip profiles have been obtained for the $(0\,0\,2)4_{3,1/2} \leftarrow (0\,0\,0)4_{4,0/1}$ doublet. By performing a wider scan around these a-type transitions, four additional resonances have been identified. Figure 8 shows the saturation signal surrounding the $(0\,0\,2)4_{3,1} \leftarrow (0\,0\,0)4_{4,0}$ transition, where the extra resonances are blue-shifted by 27.7 MHz [panel (b)] and 54.8 MHz [panel (c)]. These values coincide almost perfectly with the predicted positions of f_2 and C_2 relative to a_2, 27.3 and 54.6 MHz, respectively. The intensity of the f_2 transition, which is much smaller than that of the a_2 and c_2 lines, is strongly dependent on the intra-cavity circulating power [see panel (d)]. This intensity dependence provides further evidence for parity-pair mixing in $HD^{16}O$. The mirror image of Fig. 8(a)–(c), where the two additional resonances are red-shifted by 27.7 and 54.8 MHz from the $(0\,0\,2)4_{3,2} \leftarrow (0\,0\,0)4_{4,1}$ line, is not shown here. Since the $(0\,0\,2)4_{3,1/2}$ splitting, 8.6 GHz, is considerably larger than the Doppler width in the 7000–7350 cm^{-1} region, the cross-overs probing the upper virtual state could not be observed.

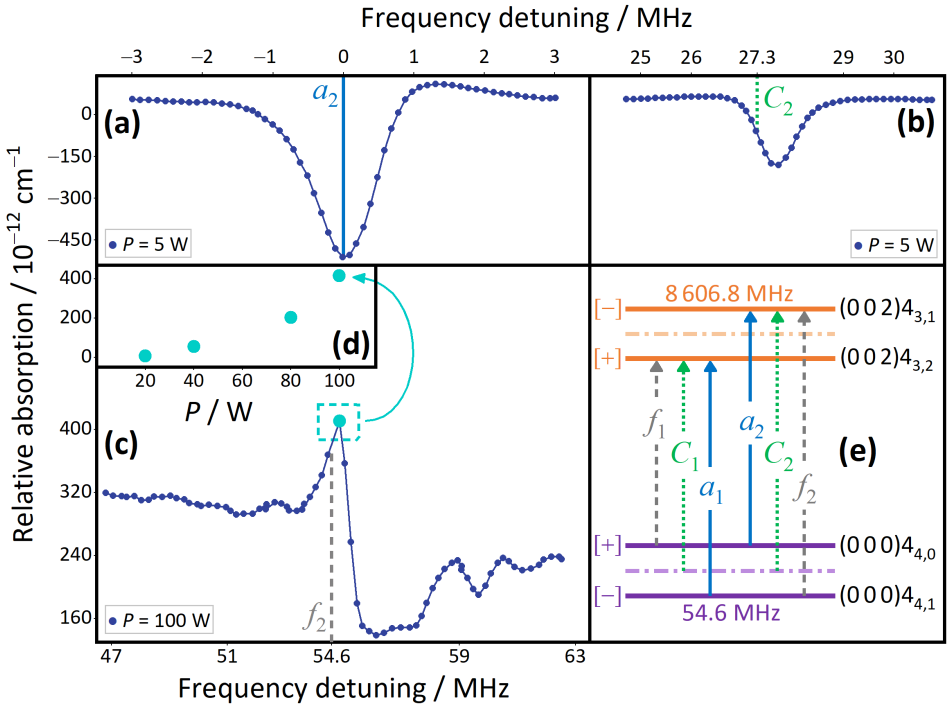

Fig. 8. Saturation spectrum recorded for the $(0\,0\,2)4_{3,1} \leftarrow (0\,0\,0)4_{4,0}$ transition. Panels (a) to (c) contain the lines corresponding to the energy-level diagram of panel (e) with resonance frequencies a_2, C_2, and f_2, respectively. Panel (d) plots the peak intensity of the dipole-forbidden f_2 line as a function of the intra-cavity laser power, P. The conventions applied in panel (e) are described in the caption to Fig. 7. The MHz values of panel (e) denote the K_c splittings of the upper and lower parity pairs. The parity of the individual states is indicated in square brackets. The vertical bars of panels (a)–(c) represent the theoretically predicted resonance positions relative to a_2, whose frequency is 213 600 053 170 kHz.

4.2.2. $(0\,0\,2)4_{4,0/1} \leftarrow (0\,0\,0)5_{5,1/0}$ doublet

Figure 9 displays the Lamb-dip spectra of the $(0\,0\,2)4_{4,0/1} \leftarrow (0\,0\,0)5_{5,1/0}$ doublet for $HD^{16}O$, $H_2{}^{16}O$ and $H_2{}^{18}O$. This parity doublet, whose energy-level scheme [see Fig. 9(g)] is an example

Optics EXPRESS

for the case reverse to that of Fig. 7(c), could not be measured in $HD^{18}O$, because its frequencies are not covered by our laser. For H_2O, single narrow Lamb dips are observed, once more demonstrating that the perturbative effects only occur in HDO, where the nuclear-spin distinction of H_2O species is lifted. In the complex Lamb-dip profile of $HD^{16}O$, the f-type transitions, f_1 and f_2, acquire almost no intensity. On the other hand, two strong c-type lines, C_1 and C_2, can be found near a_1 and a_2, respectively. The cross-overs linked with the upper virtual state, which should be in principle measurable, were not studied.

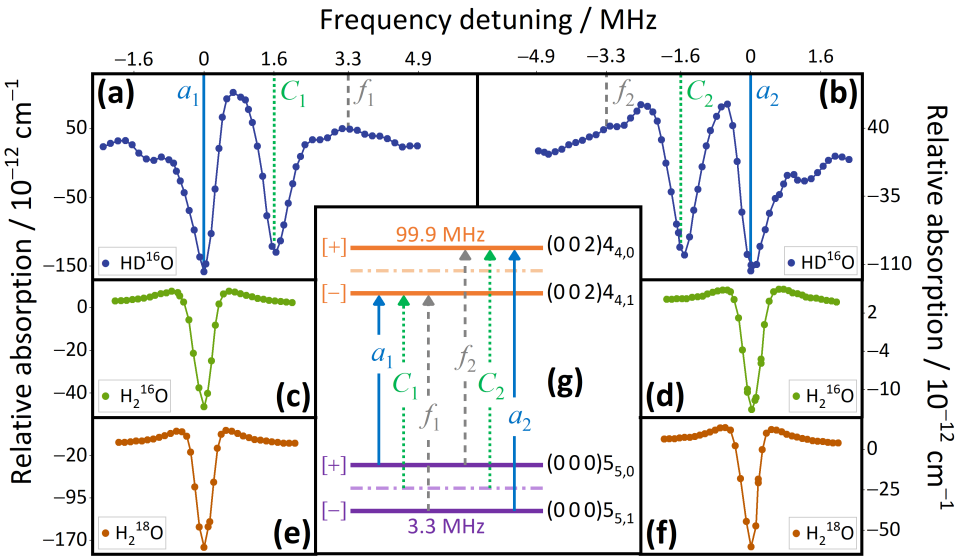

Fig. 9. Lamb dips for a close-lying parity doublet of different water isotopologues. For $HD^{16}O$, a multi-component Lamb-dip profile was detected, while the saturation spectra of $H_2^{16}O$ and $H_2^{18}O$ exhibit only a single resonance. The analogous $HD^{18}O$ line, which should be very similar to that of $HD^{16}O$, falls outside the 7000–7350 cm^{-1} region. The line centers, corresponding to zero detunings and given in kHz, are the following: 209 986 146 435 [panel (a)], 209 986 249 858 [panel (b)], 214 512 580 150 [panel (c)], 214 513 924 110 [panel (d)], 213 838 639 897 [panel (e)], and 213 840 105 039 [panel (f)]. Note the one-to-one correspondence between the vertical bars of the spectra and the arrows of the energy-level diagram of panel (g). The theoretical positions of the individual resonances are relative to a_1 [panel (a)] or a_2 [panel (b)]. For further details on the structure of the energy-level scheme, see the captions to Figs. 7 and 8.

4.2.3. $(0\,0\,2)6_{5,2/1} \leftarrow (0\,0\,0)6_{5,1/2}$ doublet

The first example for a complex Lamb-dip spectrum, where the nonuplet lines introduced in Fig. 7(c) could be unambiguously resolved, is shown in Fig. 10. In this case, the two K_c splittings are small enough (<80 MHz) to keep the extra lines within the Doppler profiles of the a-type transitions. The nine resonances, whose relative positions agree reasonably well with their theoretical estimates, are contained in a single spectrum covering a frequency range of ±60 MHz. The presence of the (higher-order) c_0 resonance, which can be considered as a novel spectral feature, could be confirmed by studying the ±10 MHz detuning window at high intracavity power [see Fig. 10(b)].

Optics EXPRESS

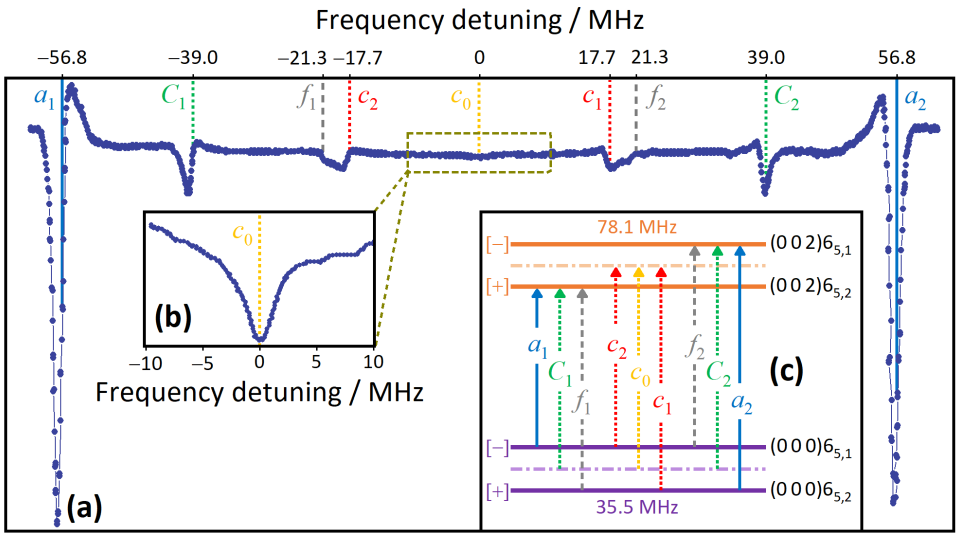

Fig. 10. Saturation spectrum involving the $(0\,0\,2)6_{5,2/1} \leftarrow (0\,0\,0)6_{5,1/2}$ doublet. Panel (a) displays a scan of ±60 MHz around the central crossover, c_0 = 215 836 700 683 kHz, corresponding to zero detuning. The environment of this c_0 line was remeasured at increased intra-cavity power, shown separately in panel (b). Note again the one-to-one correspondence between the vertical bars of the Lamb-dip spectrum [panel (a)] and the lines of the energy-level diagram [panel (c)]. The vertical bars indicate the theoretical positions of the nine lines relative to c_0. In this figure, as well as in subsequent figures, the scale of the vertical axis is not specified, because this information is not necessary to understand the spectral features observed.

4.2.4. $(0\,0\,2)5_{5,0/1} \leftarrow (0\,0\,0)6_{5,1/2}$ doublet

In the previous subsections, Lamb-dip spectra were analyzed whereby the K_c splitting is smaller for the lower-energy parity pair than for the higher-energy one [*i.e.*, $\Delta_U(K_c)>\Delta_L(K_c)$ in general terms]. The $(0\,0\,2)5_{5,0/1} \leftarrow (0\,0\,0)6_{5,1/2}$ doublet of Fig. 11 demonstrates the opposite case, with $\Delta_U(K_c)<\Delta_L(K_c)$, involving the inversions $a_1 \leftrightarrow a_2$, $C_1 \leftrightarrow c_2$, and $C_2 \leftrightarrow c_1$ in the ordering of the line positions. The a-type transitions of Fig. 11, from which the f-type lines are shifted by ±7.2 MHz, are characterized with a fairly small separation, 28.2 MHz. The f_1 and c_2 resonances are not plotted, they could not be measured due to an overlapping $H_2{}^{16}O$ line.

4.2.5. $(0\,0\,2)7_{6,1/2} \leftarrow (0\,0\,0)7_{6,2/1}$ doublet

As emphasized in Sec. 3.1, the saturation spectra of $HD^{16}O$ reach a higher degree of complexity with increased J and K_a values. Figure 12 shows an interesting example, with an energy-level scheme similar to that of Fig. 10, but with significantly smaller (<10 MHz) K_c splittings. In view of the dense structure of this multi-component spectrum, an additional measurement was performed with 3f demodulation of the NICE-OHMS signal, thereby obtaining a higher resolving power [46] as compared to the 1f detection scheme.

Although the strongest resonance is assigned to the c_0 cross-over in the 1f profile, the a-type transitions, separated by 8.6 MHz, are the most intense in the 3f recording. As in the preceding examples, the f-type components are extremely weak (in fact, they are barely detectable in the present case). The four c-type resonances are clearly visible in the 3f spectrum and agree particularly well with the theoretical positions relative to c_0. The two green cross-overs, C_1 and C_2, appear as Lamb-dips, while the red lines, c_1 and c_2, produce Lamb peaks, a typical

Optics EXPRESS

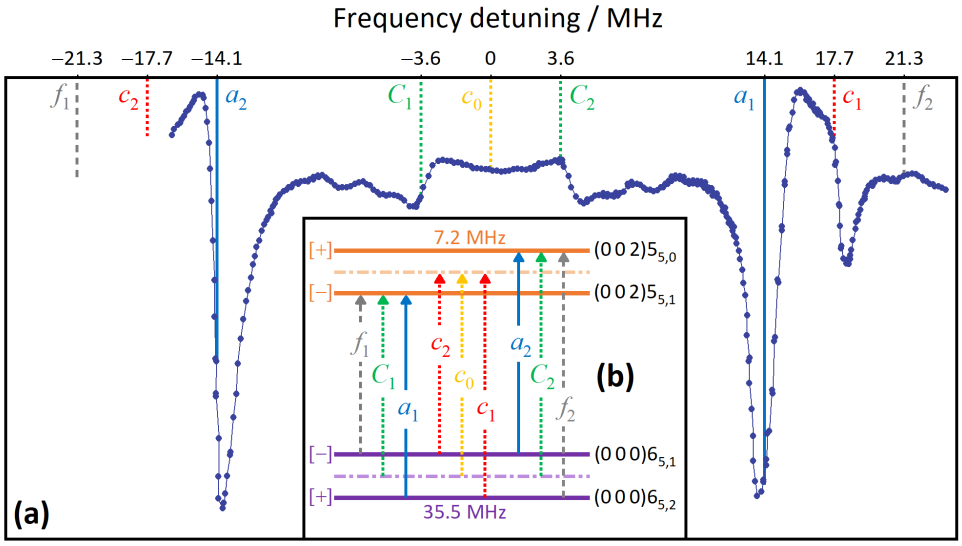

Fig. 11. Lamb-dip spectrum detected for the $(0\,0\,2)5_{5,0/1} \leftarrow (0\,0\,0)6_{5,1/2}$ doublet. Note the one-to-one correspondence between the vertical bars of the spectrum [panel (a)] and the lines of the energy-level diagram [panel (b)]. The vertical bars provide the theoretical positions of the nine lines relative to the c_0 resonance coinciding with the line center at 213 065 604 238 kHz. The detuning region below −13 MHz, which is overlapped with the $(2\,0\,0)1_{1,0} \leftarrow (0\,0\,0)2_{2,1}$ transition of $H_2^{16}O$, is not presented. Since the K_c splitting is larger for the lower-energy parity pair, the ordering of the nine resonances is different from that of Fig. 10 (fact, the difference is connected to the $a_1 \leftrightarrow a_2$, $C_1 \leftrightarrow c_2$, and $C_2 \leftrightarrow c_1$ inversions).

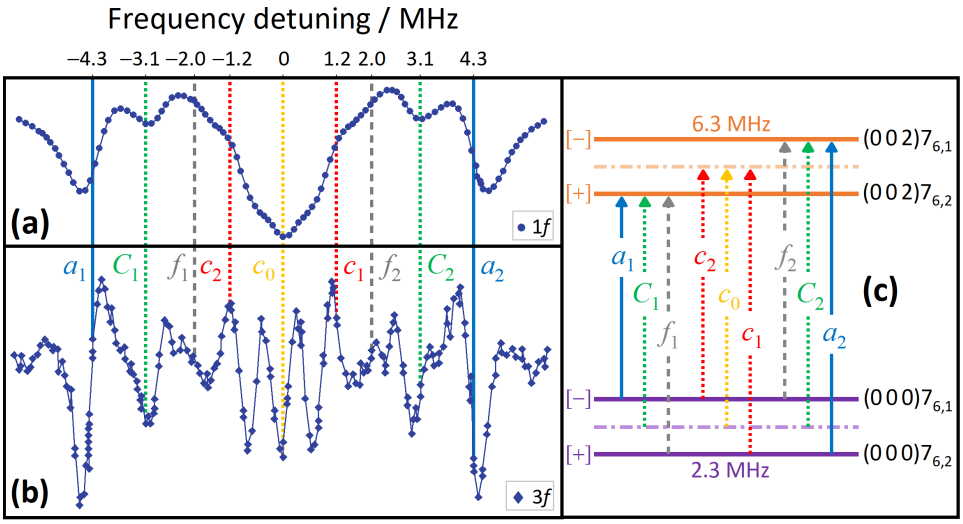

Fig. 12. Lamb-dip spectrum recorded for the $(0\,0\,2)7_{6,1/2} \leftarrow (0\,0\,0)7_{6,1/2}$ doublet. Panels (a) and (b) are related to $1f$ and $3f$ demodulation signals, respectively. The nine resonances, which appear to be better resolved in the $3f$ spectrum, are associated with the lines of the energy-level scheme of panel (c). As in Figs. 10 and 11, the theoretical positions marked with vertical bars are relative to the central resonance, c_0 = 215 196 861 851 kHz. As clear from panels (a) and (b), the Lamb dips of the a-type transitions are somewhat shifted from the theoretical predictions.

Optics EXPRESS

sign-reversing effect in saturation spectroscopy [40]. In the 3f spectrum, further resonances are also observed, for which no assignment can be given based on our semi-quantitative model.

4.2.6. $(0\,0\,2)8_{7,1/2} \leftarrow (0\,0\,0)7_{6,2/1}$ and $(0\,0\,2)8_{7,1/2} \leftarrow (0\,0\,0)7_{7,0/1}$ doublets

During this study, a large number of Lamb dips were found mimicking a double-spike phenomenon, for which two examples are given in Fig. 13. For both examples, the upper states correspond to the $(0\,0\,2)8_{7,1/2}$ parity pair with a 0.6 MHz splitting. In one case [Fig. 13(a)], the lower-state K_c splitting is 2.3 MHz, while the same splitting reduces to 10 kHz in the other example [Fig. 13(b)]. Due to their fairly high intensity, the C_1, c_0, and C_2 cross-overs can be easily recognized in Fig. 13(a), but no convincing assignment emerged for the remaining resonances.

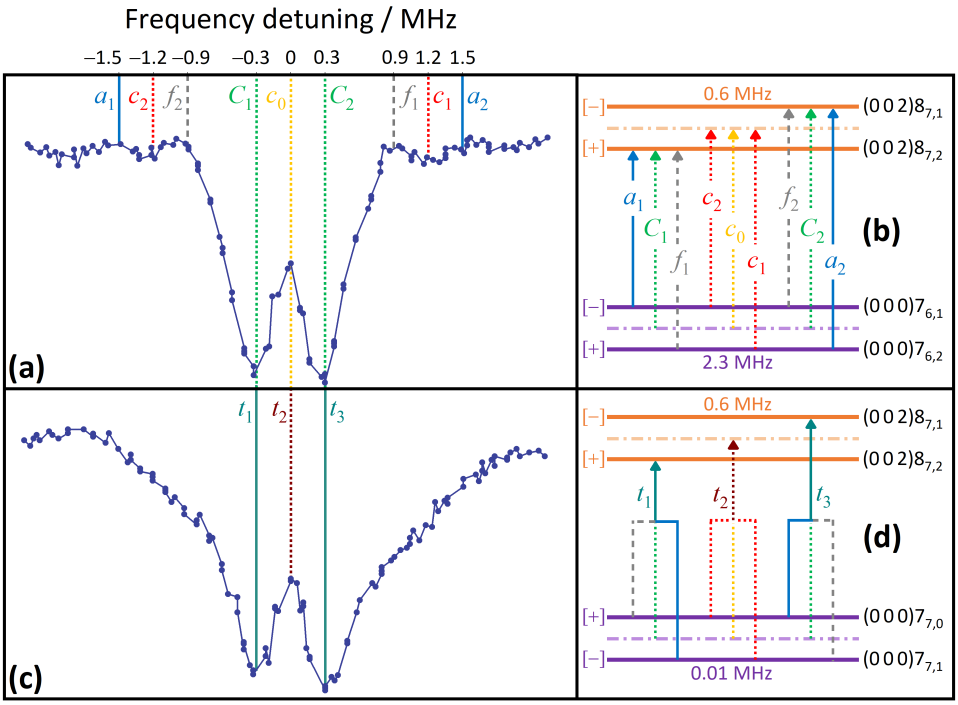

Fig. 13. Typical double-spike Lamb-dip features identified during the present study. Panels (a) and (c) visualize the saturation spectra of the $(0\,0\,2)8_{7,1/2} \leftarrow (0\,0\,0)7_{7,0/1}$ and $(0\,0\,2)8_{7,1/2} \leftarrow (0\,0\,0)7_{6,1/2}$ doublets, respectively, together with the associated energy-level schemes in panels (b) and (d), respectively. Owing to the tiny K_c splitting of the $(0\,0\,0)7_{7,0/1}$ pair, only the unresolved triplets of lines, sharing the same upper state and denoted with t_1, t_2, and t_3 [see also panel (d)], can be seen in panel (c).

As to the other doublet, the minuscule lower-state splitting leads to the coalescence of those lines with the same upper state at the current resolution of our NICE-OHMS spectrometer (200–300 kHz). Therefore, the prominent features of Fig. 13(b) can be ascribed to the t_1, t_2, and t_3 triplets defined in Fig. 13(d), which are located at detunings of –0.3, 0, and 0.3 MHz, respectively. In those cases when both splittings become smaller 200 kHz, only a single-spike feature, resembling a regular Lamb-dip with some spectral distortions, can be detected with our setup.

Optics EXPRESS

5. Conclusions

Motivated by our previous studies on $H_2{}^{16}O$ [9,13] and $H_2{}^{18}O$ [10], the original aim of this study was the derivation of kHz-accuracy energy levels within the ground vibrational state of $HD^{16}O$, by measuring near-infrared transitions *via* the NICE-OHMS saturation-spectroscopy technique. In principle, saturation spectroscopy enables the extraction of line frequencies with a few kHz uncertainty, corresponding to a 100–1000 times improvement in comparison to the MHz-level accuracy of Doppler-broadened approaches. Previously, over 50 000 rovibrational lines have been detected for $HD^{16}O$, linking some 10 000 of its quantum states in the electronic ground state [28,47].

In the present study, Lamb dips were recorded for more than 100 rovibrational transitions in the first overtone of the O–H stretch fundamental of $HD^{16}O$, yielding line positions with an experimental reproducibility of 2–20 kHz. For transitions with $\max(K_a', K_a'')>3$, multi-component Lamb-dip profiles with highly varying complexity were observed. Analyzing the experimental (NICE-OHMS-based) K_c splittings of parity pairs (that is, pairs of opposite-parity energy levels differing only in their K_c values) in the ground vibrational state, significant deviations were identified from predictions provided by an accurate effective-Hamiltonian (EH) model [19]. Even in view of the frequency shifts revealed, the line centers of symmetric Lamb dips still have an absolute accuracy on the order of 100 kHz, leading to a ten times improvement with respect to the uncertainties of Doppler-limited $HD^{16}O$ lines.

The spectral perturbations discovered in the Lamb-dip profiles of $HD^{16}O$ transitions can be semi-quantitatively described by assuming that an (optical) AC-Stark effect causes mixing between the states of parity pairs. This assumption was verified by measuring transition doublets with the same assignment for four water isotopologues: $H_2{}^{16}O$, $H_2{}^{18}O$, $HD^{16}O$, and $HD^{18}O$. The comparison of the results obtained for the different species suggests that (a) there is no perturbation in the near-infrared Lamb-dip spectra of $H_2{}^{16}O$ and $H_2{}^{18}O$, and (b) the perturbative effects are equally present in $HD^{16}O$ and $HD^{18}O$. The reason behind the dissimilar behavior of H_2O and HDO is that the parity pairs of H_2O are *ortho–para* nuclear-spin-isomer pairs, preventing their significant interaction. This means that the distortion effects are related to the reduction of the molecular symmetry under the H→D replacement. Moreover, it is shown that the multi-component spectral features are not caused by the sidebands of the NICE-OHMS technique, but result from saturation spectroscopy as such.

To establish a semi-quantitative model, a general four-state scheme of two parity pairs is presented, explaining the appearance of extra resonances in the saturation spectra of HDO. In this scheme, four infrared lines (two dipole-allowed and two dipole-forbidden) are specified, where parity-pair mixing yields intensity for the two dipole-forbidden transitions, making them quantum mechanically allowed. Furthermore, cross-over resonances, previously observed in non-linear spectroscopy but not in connection to parity-pair mixing of polyatomic molecules, may also occur in the multi-component Lamb-dip profiles of HDO, leading to altogether nine near-infrared resonances in our four-state scheme.

As illustrated for eight transition doublets, the experimental positions of the nine resonances, relative to the central cross-over, agree reasonably well with their theoretical (EH-predicted and/or variationally-computed) counterparts. Thus, the good matches between the experimental and theoretical relative positions confirm the assignments provided for the individual frequency components. The theoretical predictions also helped to find the weak forbidden lines for the $(0\,0\,2)3_{2,1/2} \leftarrow (0\,0\,0)3_{3,0/1}$ transition doublet (see Supplement 1 [39] Sec. S2), whose lines exhibit symmetric saturation spectra, but their frequency shifts are larger than 90 kHz. These weak signals demonstrate that the AC-Stark perturbations occur even in those cases when there is no asymmetry around the Lamb dips of the dipole-allowed transitions.

Although our four-state scheme provides unique assignments for the resonances of complex saturation spectra in HDO, a sophisticate quantum-chemical model is needed for a fully quantitative

Optics EXPRESS

description of the multi-component Lamb-dip profiles and the frequency shifts observed. This model should consider (a) the usual conditions applied in saturation spectroscopy, (b) the dynamic coupling between lower and upper states by the laser field, (c) the AC-Stark interaction between the two states of parity pairs, and (d) the $2J + 1$ Stark-induced "sub-levels" of the rovibrational states [36,48]. A set of optical Bloch equations, involving the possible sub-levels, might deal with all the coherences, also including cross-over resonances, as shown recently for HD [17] and for general multi-state interaction schemes [49,–51]. Since the cited papers investigate interactions between states with the same parity, their formulas cannot be employed directly for the complex Lamb-dip shapes of HDO, where the AC-Stark effect takes place between the two energy levels of parity pairs.

Funding. Nederlandse Organisatie voor Wetenschappelijk Onderzoek (16MYSTP); Nemzeti Kutatási Fejlesztési és Innovációs Hivatal (K138233); Horizon 2020 Framework Programme (654148).

Acknowledgments. The authors thank Prof. Ad van der Avoird (Radboud University Nijmegen) for insightful discussions on the symmetries of quantum states of water isotopologues.

Disclosures. The authors declare no conflicts of interest.

Data availability. Data underlying the results presented in this paper are available in Dataset 1 [33] and Dataset 2 [34].

Supplemental document. See Supplement 1 for supporting content.

References

1. M. Quack and F. Merkt, eds., *Handbook of High-Resolution Spectroscopy* (Wiley, 2011).
2. V. S. Letokhov and V. P. Chebotayev, *Nonlinear Laser Spectroscopy* (Springer-Verlag, 1977).
3. L.-S. Ma, J. Ye, P. Dubé, and J. L. Hall, "Ultrasensitive frequency-modulation spectroscopy enhanced by a high-finesse optical cavity: theory and application to overtone transitions of C_2H_2 and C_2HD," J. Opt. Soc. Am. B **16**(12), 2255–2268 (1999).
4. A. Foltynowicz, F. M. Schmidt, W. Ma, and O. Axner, "Noise-immune cavity-enhanced optical heterodyne molecular spectroscopy: Current status and future potential," Appl. Phys. B **92**(3), 313–326 (2008).
5. D. Gatti, R. Gotti, A. Gambetta, M. Belmonte, G. Galzerano, P. Laporta, and M. Marangoni, "Comb-locked Lamb-dip spectrometer," Sci. Rep. **6**(1), 27183 (2016).
6. J. Wang, Y. R. Sun, L.-G. Tao, A.-W. Liu, T.-P. Hua, F. Meng, and S.-M. Hu, "Comb-locked cavity ring-down saturation spectroscopy," Rev. Sci. Instrum. **88**(4), 043108 (2017).
7. H. Wu, C.-L. Hu, J. Wang, Y. R. Sun, Y. Tan, A.-W. Liu, and S.-M. Hu, "A well-isolated vibrational state of CO_2 verified by near-infrared saturated spectroscopy with kHz accuracy," Phys. Chem. Chem. Phys. **22**(5), 2841–2848 (2020).
8. Z. D. Reed, D. A. Long, H. Fleurbaey, and J. T. Hodges, "SI-traceable molecular transition frequency measurements at the 10^{-12} relative uncertainty level," Optica **7**(9), 1209–1220 (2020).
9. R. Tóbiás, T. Furtenbacher, I. Simkó, A. G. Császár, M. L. Diouf, F. M. J. Cozijn, J. M. A. Staa, E. J. Salumbides, and W. Ubachs, "Spectroscopic-network-assisted precision spectroscopy and its application to water," Nat. Commun. **11**(1), 1708 (2020).
10. M. L. Diouf, R. Tóbiás, I. Simkó, F. M. J. Cozijn, E. J. Salumbides, W. Ubachs, and A. G. Császár, "Network-based design of near-infrared Lamb-dip experiments and the determination of pure rotational energies of $H_2{}^{18}O$ at kHz accuracy," J. Phys. Chem. Ref. Data **50**(2), 023106 (2021).
11. Z. Reed, B. Drouin, D. Long, and J. Hodges, "Molecular transition frequencies of CO_2 near 1.6 μm with kHz-level uncertainties," J. Quant. Spectrosc. Radiat. Transfer **271**, 107681 (2021).
12. E. Fasci, S. Gravina, G. Porzio, A. Castrillo, and L. Gianfrani, "Lamb-dip cavity ring-down spectroscopy of acetylene at 1.4 μm," New J. Phys. **23**(12), 123023 (2021).
13. M. L. Diouf, R. Tóbiás, T. S. van der Schaaf, F. M. Cozijn, E. J. Salumbides, A. G. Császár, and W. Ubachs, "Ultraprecise relative energies in the (2 0 0) vibrational band of $H_2{}^{16}O$," Mol. Phys. **120**(15-16), e2050430 (2022).
14. R. Aiello, V. Di Sarno, M. G. D. Santi, M. De Rosa, I. Ricciardi, G. Giusfredi, P. De Natale, L. Santamaria, and P. Maddaloni, "Lamb-dip saturated-absorption cavity ring-down rovibrational molecular spectroscopy in the near-infrared," Photonics Res. **10**(8), 1803–1809 (2022).
15. M. Sinhal, A. Johnson, and S. Willitsch, "Frequency stabilisation and SI tracing of mid-infrared quantum-cascade lasers for precision molecular spectroscopy," *Mol. Phys.*, e2144519 (to be published).
16. F. M. J. Cozijn, P. Dupré, E. J. Salumbides, K. S. E. Eikema, and W. Ubachs, "Sub-Doppler frequency metrology in HD for tests of fundamental physics," Phys. Rev. Lett. **120**(15), 153002 (2018).
17. M. Diouf, F. Cozijn, B. Darquié, E. Salumbides, and W. Ubachs, "Lamb-dips and Lamb-peaks in the saturation spectrum of HD," Opt. Lett. **44**(19), 4733–4736 (2019).
18. H. W. Kroto, *Molecular Rotation Spectra* (Dover, 1992).

Optics EXPRESS

19. G. Cazzoli, V. Lattanzi, J. L. Alonso, J. Gauss, and C. Puzzarini, "The hyperfine structure of the rotational spectrum of HDO and its extension to the THz region: Accurate rest frequencies and spectroscopic parameters for astrophysical observations," Astrophys. J. **806**(1), 100 (2015).
20. D. Romanini, I. Ventrillard, G. Méjean, J. Morville, and E. Kerstel, "Introduction to cavity enhanced absorption spectroscopy," in *Cavity-Enhanced Spectroscopy and Sensing*, (Springer, 2014), pp. 1–60.
21. H. Dinesan, E. Fasci, A. d'Addio, A. Castrillo, and L. Gianfrani, "Characterization of the frequency stability of an optical frequency standard at 1.39 µm based upon noise-immune cavity-enhanced optical heterodyne molecular spectroscopy," Opt. Express **23**(2), 1757–1766 (2015).
22. S. Twagirayezu, M. J. Cich, T. J. Sears, C. P. McRaven, and G. E. Hall, "Frequency-comb referenced spectroscopy of ν_4- and ν_5-excited hot bands in the 1.5 µm spectrum of C_2H_2," J. Mol. Spectrosc. **316**, 64–71 (2015).
23. E. B. Treacy and Y. Beers, "Hyperfine structure of the rotational spectrum of HDO," J. Chem. Phys. **36**(6), 1473–1480 (1962).
24. P. Thaddeus, L. C. Krisher, and J. H. N. Loubser, "Hyperfine structure of the microwave spectrum of HDO, HDS, CH_2O, and CHDO: beam-maser spectroscopy and asymmetric-top molecules," J. Chem. Phys. **40**(2), 257–273 (1964).
25. H. Bluyssen, J. Verhoeven, and A. Dymanus, "Hyperfine structure of HDO and D_2O by beam maser spectroscopy," Phys. Lett. A **25**(3), 214–215 (1967).
26. S. G. Kukolich, "Beam maser double resonance measurements on HDO," J. Chem. Phys. **66**(10), 4345–4348 (1977).
27. H. A. Fry and S. G. Kukolich, "Beam maser measurements of HDO hyperfine structure," J. Chem. Phys. **76**(9), 4387–4391 (1982).
28. J. Tennyson, P. F. Bernath, and L. R. Brown, *et al.*, "IUPAC critical evaluation of the rotational-vibrational spectra of water vapor. Part II. Energy levels and transition wavenumbers for $HD^{16}O$, $HD^{17}O$, and $HD^{18}O$," J. Quant. Spectrosc. Radiat. Transfer **111**(15), 2160–2184 (2010).
29. E. Mátyus, G. Czakó, and A. G. Császár, "Toward black-box-type full- and reduced-dimensional variational (ro)vibrational computations," J. Chem. Phys. **130**(13), 134112 (2009).
30. C. Fábri, E. Mátyus, and A. G. Császár, "Rotating full- and reduced-dimensional quantum chemical models of molecules," J. Chem. Phys. **134**(7), 074105 (2011).
31. C. Fábri, M. Quack, and A. G. Császár, "On the use of nonrigid-molecular symmetry in nuclear-motion computations employing a discrete variable representation: a case study of the bending energy levels of CH_5^+," J. Chem. Phys. **147**(13), 134101 (2017).
32. P. Barletta, S. V. Shirin, N. F. Zobov, O. L. Polyansky, J. Tennyson, E. F. Valeev, and A. G. Császár, "CVRQD *ab initio* ground-state adiabatic potential energy surfaces for the water molecule," J. Chem. Phys. **125**(20), 204307 (2006).
33. M. L. Diouf, R. Tóbiás, F. M. J. Cozijn, E. J. Salumbides, C. Fábri, C. Puzzarini, A. G. Császár, and W. Ubachs, "Parity-pair-mixing effects in nonlinear spectroscopy of HDO," figshare (2022), https://doi.org/10.6084/m9.figshare.20728444 Dataset 1.
34. M. L. Diouf, R. Tóbiás, F. M. J. Cozijn, E. J. Salumbides, C. Fábri, C. Puzzarini, A. G. Császár, and W. Ubachs, "Parity-pair-mixing effects in nonlinear spectroscopy of HDO," figshare (2022), https://doi.org/10.6084/m9.figshare.20728552 Dataset 2.
35. C. E. Otis and P. M. Johnson, "The AC-Stark effect in molecular multiphoton ionization spectroscopy," Chem. Phys. Lett. **83**(1), 73–77 (1981).
36. W. M. Huo, K. P. Gross, and R. L. McKenzie, "Optical Stark effect in the two-photon spectrum of NO," Phys. Rev. Lett. **54**(10), 1012–1015 (1985).
37. C. Wieman, M. Noecker, B. Masterson, and J. Cooper, "Asymmetric line shapes for weak transitions in strong standing-wave fields," Phys. Rev. Lett. **58**(17), 1738–1741 (1987).
38. J. E. Stalnaker, D. Budker, S. Freedman, J. Guzman, S. Rochester, and V. Yashchuk, "Dynamic Stark effect and forbidden-transition spectral line shapes," Phys. Rev. A **73**(4), 043416 (2006).
39. M. L. Diouf, R. Tóbiás, F. M. J. Cozijn, E. J. Salumbides, C. Fábri, C. Puzzarini, A. G. Császár, and W. Ubachs, "Parity-pair-mixing effects in nonlinear spectroscopy of HDO," (2022), https://doi.org/10.6084/m9.figshare.21520698 Supplement 1.
40. W. Demtröder, *Laser Spectroscopy: Vol. 2 Experimental Techniques* (Springer, 2021).
41. H. J. Foth and F. Spieweck, "Hyperfine structure of the R(98), 58-1 line of $^{127}I_2$ at 514.5 nm," Chem. Phys. Lett. **65**(2), 347–352 (1979).
42. L. Julien, M. Pinard, and F. Laloë, "Hyperfine structure and isotope shift of the 640.2 and 626.6 nm lines of neon," J. Phys., Lett. **41**(20), 479–482 (1980).
43. L. Bloomfield, H. Gerhardt, T. Hansch, and S. Rand, "Nonlinear UV-laser spectroscopy of the 2^3S–5^3P transition in ^3He and ^4He," Opt. Commun. **42**(4), 247–250 (1982).
44. A. Schabert, R. Keil, and P. Toschek, "Dynamic Stark effect of an optical line observed by cross-saturated absorption," Appl. Phys. **6**(2), 181–184 (1975).
45. C. Hertzler and H.-J. Foth, "Sub-Doppler polarization spectra of He, N_2 and Ar^+ recorded in discharges," Chem. Phys. Lett. **166**(5-6), 551–559 (1990).
46. M. Melosso, M. L. Diouf, L. Bizzocchi, M. E. Harding, F. M. J. Cozijn, C. Puzzarini, and W. Ubachs, "Hyperfine-resolved near-infrared spectra of $H_2{}^{17}O$," J. Phys. Chem. A **125**(36), 7884–7890 (2021).

Optics EXPRESS

47. A. A. Kyuberis, N. F. Zobov, O. V. Naumenko, B. A. Voronin, O. L. Polyansky, L. Lodi, A. Liu, S.-M. Hu, and J. Tennyson, "Room temperature line lists for deuterated water," J. Quant. Spectrosc. Radiat. Transfer **203**, 175–185 (2017).
48. J. S. Bakos, "AC Stark effect and multiphoton processes in atoms," Phys. Rep. **31**(3), 209–235 (1977).
49. S. Mandal and P. N. Ghosh, "Line shape and frequency shift of Lamb dip and crossover-resonance dip in closely spaced transitions," Phys. Rev. A **45**(7), 4990–4997 (1992).
50. S. Mandal and P. N. Ghosh, "Line shape, frequency shift, Rabi splitting, and two-photon resonances in four-level double-resonance spectroscopy with closely spaced intermediate levels," Phys. Rev. A **47**(6), 4934–4945 (1993).
51. S. Ghosh and S. Mandal, "Analytical studies on pump-induced optical resonances in an *M*-type six-level system," J. Phys. B: At., Mol. Opt. Phys. **43**(24), 245505 (2010).